Journal of Alloys and Compounds xxx (xxxx) xxx

Contents lists available at ScienceDirect

Journal of Alloys and Compounds

journal homepage: http://www.elsevier.com/locate/jalcom

High pressure phase of Ba_2FeS_3: An antiferromagnet with one-dimensional spin chains

Lei Duan [a, b, c, 1], Jun Zhang [a, c, 1], Xiancheng Wang [a, c, *], Zhiwei Zhao [b], Changjiang Xiao [b], Xiang Li [d], Zhiwei Hu [e], Jianfa Zhao [a, c], Wenmin Li [a, c], Lipeng Cao [a, c], Guangyang Dai [a, c], Chongwen Ren [a, c], Xin He [a, c], Runze Yu [a], QingQing Liu [a], Liu Hao Tjeng [e], Hong-Ji Lin [f], Chien-Te Chen [f], Changqing Jin [a, c, g, **]

[a] Beijing National Laboratory for Condensed Matter Physics, Institute of Physics, Chinese Academy of Sciences, Beijing, 100190, China
[b] College of Materials Science and Engineering, Henan University of Technology, Zhengzhou, 450001, China
[c] School of Physics, University of Chinese Academy of Sciences, Beijing, 100190, China
[d] Key Laboratory of Advanced Optoelectronic Quantum Architecture and Measurement, School of Physics, Beijing Institute of Technology, Beijing, 100081, China
[e] Max Plank Institute for Chemical Physics of Solids, Nöthnitzer Strasse 40, D-01187, Dresden, Germany
[f] National Synchrotron Radiation Research Center, Hsinchu, 30076, Taiwan
[g] Materials Research Lab at Songshan Lake, Dongguan, 523808, China

ARTICLE INFO

Article history:
Received 5 August 2020
Received in revised form
12 October 2020
Accepted 29 October 2020
Available online xxx

Keywords:
One-dimensional spin chain
High pressure
Antiferromagnet
Semiconductor

ABSTRACT

In this work, we report on the discovery of the high-pressure phase of Ba_2FeS_3 with quasi one-dimensional (1D) spin chains, which was synthesized under high-pressure and high-temperature conditions. A systematic study was carried out via structural, transport, magnetic and thermodynamic measurements. The high-pressure phase of Ba_2FeS_3 (denoted by Ba_2FeS_3 (HP)) crystallizes in a K_2AgI_3-typed orthorhombic structure with the space group of *Pnma* (62) and the lattice parameters of $a = 8.6831$ (1) Å, $b = 4.2973$ (1) Å, and $c = 17.0254$ (2) Å, respectively, which consists of chains of corner-sharing FeS_4 tetrahedra along the b axis. Ba_2FeS_3 (HP) undergoes a long-range antiferromagnetic transition at T_N ~56 K, above which the magnetic susceptibility curve exhibits a round hump behavior with the maximum temperature T_{max} ~110 K. In addition, the intrachain coupling J_{intra} is about −18 K obtained by using the Wagner-Friedberg model. The specific heat data suggest that the total magnetic entropy change ΔS caused by the long-range ordering transition is only ~20% of the expected value for a $S = 2$ system. For comparison, the properties of K_2CuCl_3-typed Ba_2FeS_3 with similar quasi 1D spin chains were presented as well. Our results indicate that both compounds exhibit a typical feature expected for compounds with 1D spin chains.

1. Introduction

The discovery of superconductivity (SC) in La(O,F)FeAs has stimulated great interest in exploring new iron based superconductor (IBS) and studying the mechanism of SC [1–5]. Most of the IBSs contain anti-PbO type FeAs/Se layers, where antiferromagnetic order and superconductivity compete with each other. FeSe is an important member of the IBSs, which crystallizes in a simple layered structure. The bulk FeSe displays SC with relatively low T_c ~8.5 K [4]. Although the static magnetic order is absent at ambient pressure, strong spin fluctuations have been identified and support the proposal that SCis closely related with magnetism [6]. In addition, many iron chalcogenides superconductors can be derived from FeSe by intercalating some alkali-metal ions and other molecules in between FeSe layers and the T_c can be enhanced to 30–40 K [7–9], such as $K_xFe_2Se_2$ [7] and (Li (1-x)Fe(x))OHFeSe [9]. Beside the layered structure, the FeS/Se_4 tetrahedrons in $BaFe_2S/Se_3$ and $(Rb,Cs)Fe_2S/Se_3$ are edge-sharing to form spin-ladders [10–14]. Interestingly, $BaFe_2S_3$ and $BaFe_2Se_3$ were reported to be

* Corresponding author. Beijing National Laboratory for Condensed Matter Physics, Institute of Physics, Chinese Academy of Sciences, Beijing, 100190, China.
** Corresponding author. Beijing National Laboratory for Condensed Matter Physics, Institute of Physics, Chinese Academy of Sciences, Beijing, 100190, China.
E-mail addresses: wangxiancheng@iphy.ac.cn (X. Wang), jin@iphy.ac.cn (C. Jin).
[1] These authors contributed equally.

https://doi.org/10.1016/j.jallcom.2020.157839
0925-8388/

superconducting after the suppress of their antiferromagnetic (AFM) order by pressure [10–12]. It seems that the SC can be achieved in iron based compounds with various structure motifs, and the compounds should contain FeS/Se_4 tetrahedron complex, which was predicted to be favored by SC [15]. As a part of ongoing research on the role of dimensionality in SC, it is interesting to look for other quasi 1D iron chalcogenides with FeS/Se_4 tetrahedral complex and AFM state beyond the ladder motif.

Besides temperature and composition, pressure is another key parameter to contribute increasingly to innovations in materials sciences [16,17]. High pressure is a powerful tool to explore new materials with exotic properties, which cannot be obtained under ambient pressure [18–20]. Here, we report the discovery of the iron-based compound Ba_2FeS_3 with chains of corner-sharing FeS_4 tetrahedra, which was synthesized under high pressure and high temperature conditions (so denoted with Ba_2FeS_3 (HP)). In addition, we notice that Ba_2FeS_3 with different structure but similar FeS_4 tetrahedral chains also can be obtained at ambient pressure (called Ba_2FeS_3 (AP)) [21]. However, the study of Ba_2FeS_3 (AP) is limited. Therefore, we demonstrate a systematic study on both Ba_2FeS_3 (HP) and Ba_2FeS_3 (AP).

2. Experimental

Commercially available crystalline powders of FeS (Alfa, 99.99%) and S (Alfa, 99.99%), and lumps of Ba (Alfa, immersed in oil, >99.2% pure) were used as starting materials. The compound of Ba_2FeS_3 (AP) was prepared via solid reaction under ambient pressure. The precursor BaS was prepared through the reaction of the Ba blocks and the S powder at 600 °C for 20 h, which were put into an alumina crucible and sealed in an evacuated quartz tube. The mixture of BaS and FeS was homogenously mixed according to a molecular ratio of 2:1. To obtain the sample of Ba_2FeS_3 (AP), the mixture was sintered at 700 °C for 20 h in an evacuated quartz tube. The high-pressure phase of Ba_2FeS_3 (HP) was synthesized under high pressure condition. Either the obtained Ba_2FeS_3 (AP) or the mixture of BaS and FeS was pressed into a pellet with a diameter of 6 mm, and then subjected to high-pressure synthesis under 5.5 GPa pressure and 1000 °C for 40 min in a cubic-anvil-type high-pressure apparatus, of which the details have been reported in ref (22,23) [22,23].

The powder x-ray diffraction was performed on a Huber diffractometer (Cu-Kα_1 radiation, 40 kV, 30 mA). The Rietveld refinement on the diffraction data was carried out by using Gsas software packaged. The *dc* magnetic susceptibility was measured using a superconducting quantum interference device (SQUID). The electronic conductivity and specific heat were measured using a physical property measuring system (PPMS). Soft X-ray absorption spectroscopy (XAS) at the Fe $L_{2,3}$-edges of Ba_2FeS_3(AP) and Ba_2FeS_3(HP) was performed at beamline BL11A of the NSRRC in Taiwan using the total electron yield mode. A Fe_2O_3 single crystal was simultaneously measured for energy reference.

3. Results and discussions

3.1. Crystal structure

The Ba_2FeS_3(HP) sample was synthesized under high-pressure and high-temperature conditions. Fig. 1(a) shows the X-ray diffraction pattern of Ba_2FeS_3 (HP). All the peaks can be indexed with an orthorhombic structure with the lattice constants of $a = 8.6831$ (1) Å, $b = 4.2973$ (1) Å, and $c =$ 17.0254 (2) Å. Here, the structure of Ba_2MnS_3 with the space group of *Pnma* (62) was adopted as the initial model for the refinements on the diffraction pattern of Ba_2FeS_3(HP) [24]. The

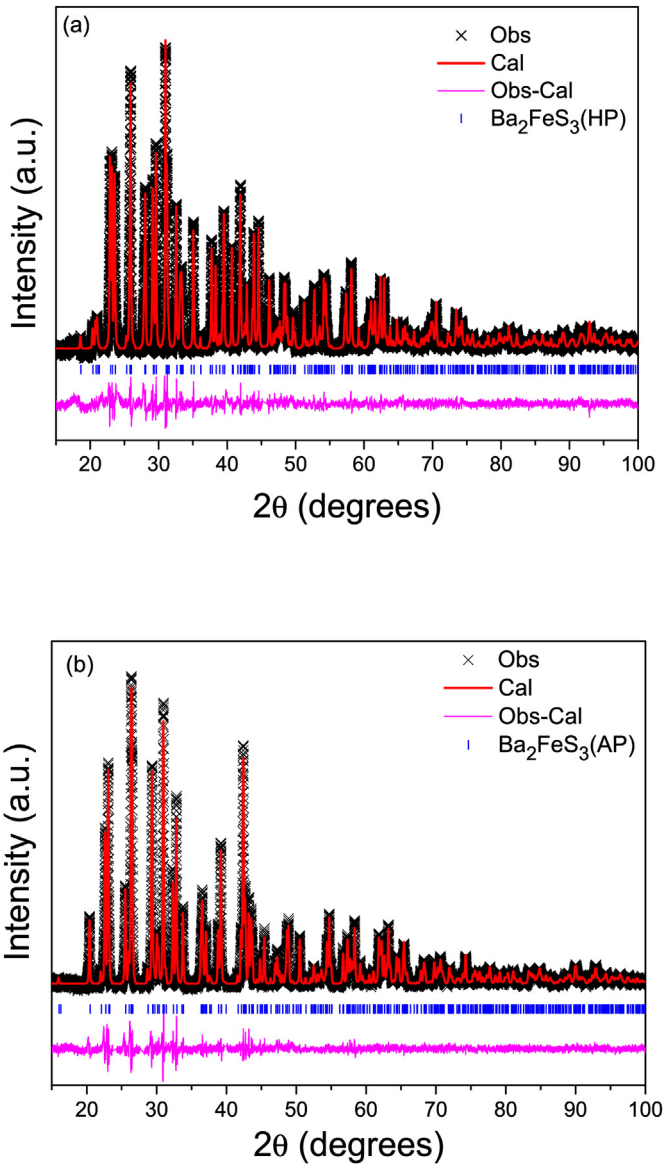

Fig. 1. The powder X-ray diffraction patterns of (a) Ba_2FeS_3(HP) and (b) Ba_2FeS_3(AP) compounds measured at room temperature and the refinements with the space group of *Pnma* (62) using Gsas software packages.

refinement smoothly converges to $R_{wp} = 3.41\%$, $R_p = 3.11\%$ and $\chi^2 = 4.3$. The crystal data and structural refinement of Ba_2FeS_3(HP) at room temperature are shown in Table 1. Some selected interatomic distances and angles are demonstrated in Table 2. For comparing, the sample of Ba_2FeS_3(AP) was also synthesized at ambient pressure and the X-ray diffraction pattern was presented in Fig. 1(b). After the refinement, the crystallographic data of Ba_2FeS_3(AP) were obtained with the lattice constants of $a = 12.1043$ (2) Å, $b = 4.2494$ (1) Å and $c = 12.3967$ (2) Å, which agrees well with the previous reports [21], and some interatomic distances are also shown in Table 2. The unit cell volume of Ba_2FeS_3(HP) is 635.28 (2) $Å^3$, which is slightly smaller than that of 637.63 (2) $Å^3$ for Ba_2FeS_3(AP).

The sketch of the crystal structures with the supercell of $1 \times 3 \times 1$ of Ba_2FeS_3(HP) and Ba_2FeS_3(AP) are displayed in Fig. 2(a and b) from the perspective view with the projection along the *b* axis, respectively. The main feature is the chain structure composed of chains of corner-sharing FeS_4 tetrahedra along the *b* axis, which

Table 1
The summary of the crystallographic data at room temperature for Ba_2FeS_3(HP).

Compound:						Ba_2FeS_3(HP)
Space group: *Pnma* (62) − orthorhombic a = 8.6831 (1) Å b = 4.2973 (1) Å c = 17.0254 (2) Å V = 635.28 (2) Å^3 Z = 4 χ^2 = 4.3 R_{wp} = 3.41% R_p = 3.11%						
Atom	Wyck	x/a		y/b	z/c	SOF U (Å^2)
Ba1	4c	0.4111 (4)		0.25	0.7119 (7)	1 0.008 (0)
Ba2	4c	0.2499 (3)		0.25	0.4540 (9)	1 0.015 (3)
Fe	4c	0.3728 (6)		0.25	0.1345 (1)	1 0.010 (6)
S1	4c	0.3343 (4)		0.25	0.2723 (5)	1 0.012 (5)
S2	4c	0.1353 (0)		0.25	0.0672 (2)	1 0.016 (1)
S3	4c	1.008 (7)		0.25	0.6029 (9)	1 0.019 (7)

Table 2
Selected interatomic distances(Å) and angles (°) for Ba_2FeS_3(HP) and Ba_2FeS_3(AP).

Compound	Ba_2FeS_3(HP)	Ba_2FeS_3(AP)
Fe−S1	2.3595 (2)	2.3278 (1)
Fe−S2	2.3705 (1)	2.2870 (2)
Fe−S3	2.4415 (1)	2.4264 (3)
Fe−Fe (intrachain)	4.2973 (1)	4.2494 (1)
Fe−Fe (interchain)	5.5199 (0)	6.2123 (1)
	5.8578 (1)	6.5538 (1)
S3−Fe−S3	123.3 (0)	122.2 (4)

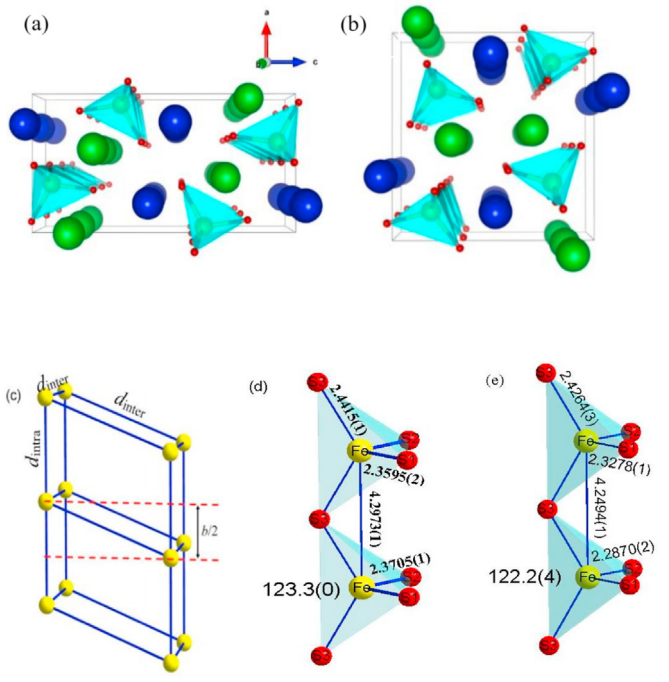

Fig. 2. (a) and (b) is the sketch of the crystal structures with supercell of 1 × 3 × 1 from the perspective view with the projection along the *b* axis for Ba_2FeS_3(HP) and Ba_2FeS_3(AP), respectively. (c) Shows the shift by the *b*/2 vector of Fe chains in the unit cell. (d) and (e) shows the tetrahedral FeS_4 chains in details for Ba_2FeS_3(HP) and Ba_2FeS_3(AP), respectively. Yellow denotes Fe atoms, green for Ba (1), blue for Ba (2) and red for S. (For interpretation of the references to colour in this figure legend, the reader is referred to the Web version of this article.)

are separated by Ba^{2+} cations. Fig. 2(c–e) presents the chains in details. In the unit cell of *ac*-plane, there are four FeS_4 chains, two of which are shifted by the *b*/2 vector, as shown in Fig. 2(c). For Ba_2FeS_3(HP), the distance of adjacent Fe^{2+} ions in the chain d_{intra} is given by the lattice constant of b = 4.2973 (1) Å; while the distance of nearest neighbor interchain Fe^{2+} ions d_{inter} is about 5.5199 (0) Å. In the zigzag-like line of -S-Fe-S-Fe- as shown in Fig. 2(d), the bond length of $L_{Fe\text{-}S3}$ is 2.4415 (1) Å and the bond angle $\alpha_{Fe\text{-}S\text{-}Fe}$ = 123.3 (0) °. It is noted that the values of d_{intra} is much larger than that of the metallic bond length of Fe−Fe (~2.425 Å), which suggests that the 3*d* orbitals of Fe ions in the chain have no direct overlap and the unpaired spins can only couple with each other via S anion. Fig. 2(e) shows the zigzag-like line of -S-Fe-S-Fe- for Ba_2FeS_3(AP). The intrachain distance d_{intra} is 4.2494 (1) Å, while the interchain distance d_{inter} in Ba_2FeS_3(AP) is 6.2123 (1) Å. Compared with Ba_2FeS_3(AP), Ba_2FeS_3(HP) has a smaller interchain distance d_{inter} but a larger intrachain distance d_{intra}. That is, after high-pressure sintering, the structure of Ba_2FeS_3(HP) is compressed in the *ac*-plane; while it is stretched along the chain direction. In addition, Ba_2FeS_3(HP) has longer Fe−S distances than Ba_2FeS_3(AP), which is suggested to arise from its more distorted FeS_4 tetrahedron and less hybridization between Fe-3*d* and S-3*p*.

For both Ba_2FeS_3(HP) and Ba_2FeS_3(AP), in terms of the cation Ba^{2+}, it is surrounded by seven coordinating S atoms, forming monocapped trigonal prisms of BaS_7, which are stacked along the *b* axis to form face-sharing Ba (1)S_7 chains and edge-sharing Ba (2)S_7 chains, respectively (shown in Fig. 3(c) and (d)). The major crystallographic difference between the two structure types is the manner that the BaS_7 polyhedral chains are arranged with respect to one another. For the Ba_2FeS_3(HP) (see Fig. 3(a)), the Ba (1)S_7 and Ba (2)S_7 polyhedrons are linked with sharing the edge to form Ba (1)S_7 and Ba (2)S_7 chains along the *a* axis if viewed in the *ac*-plane. Thus, the structure of Ba_2FeS_3(HP) can be described as layered

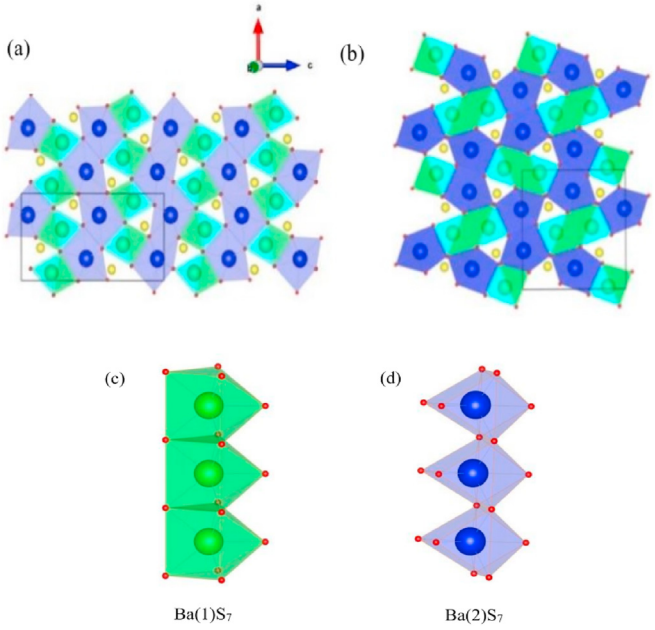

Fig. 3. (a) and (b) are the configuration of the two types of BaS_7 polyhedrons in the *ac*-plane for Ba_2FeS_3(HP) and Ba_2FeS_3(AP), respectively. (c) and (d) are the monocapped trigonal prisms of BaS_7, connected with sharing face and sharing edge, respectively. Yellow denotes Fe atoms, green for Ba (1), blue for Ba (2) and red for S. (For interpretation of the references to colour in this figure legend, the reader is referred to the Web version of this article.)

compound in terms of BaS_7 polyhedrons, where the Ba (1)S_7 and Ba (2)S_7 layers are alternately stacked along the *c* axis and the Fe atoms are inserted in between the BaS_7 layers. In contrast, in the *ac*-plane of Ba_2FeS_3(AP) (seen in Fig. 3(b)), the Ba (1)S_7 and Ba (2)S_7 polyhedrons are paired, respectively, with sharing the edge to form paring units, and the Fe atoms are surrounded by the paring units. Due to the chain-like configurations of BaS_7 polyhedrons in the *ac*-plane, Ba_2FeS_3(HP) has a smaller distance of adjacent interchain Fe atoms.

It has been reported that the alkaline-transition metal halides can crystallize in one of two closely orthorhombic K_2CuCl_3-typed and K_2AgI_3-typed structures, which is determined by the ionic radius ratio of r_M/r_A (*M* demotes the transition metal and *A* for alkaline metal) [25]. A larger ratio generally leads to K_2AgI_3-typed structure. Moreover, for Ba_2MS_3 family the ratio of $r_{M^{2+}}/\ r_{Ba^{2+}}$ dependence of structure type has been studied [26]. It was found that the compounds with small ionic radius of M^{2+} adopt K_2CuCl_3-typed structure, such as Ba_2CoS_3 with $r_{Co^{2+}} \sim 0.58$ Å; for a large ionic radius of M^{2+}, the compounds crystallize in K_2AgI_3-typed structure, such as Ba_2MnS_3 ($r_{Mn^{2+}} \sim 0.66$ Å), whereas a moderate ionic radius M^{2+} can lead to either K_2CuCl_3-typed or K_2AgI_3-typed structure, such as Ba_2ZnS_3 $r_{Zn^{2+}} \sim 0.60$ Å. Ba_2ZnS_3 with K_2CuCl_3-typed structure can be obtained via ambient pressure synthesis, while it crystallizes in K_2AgI_3-typed structure if it is synthesized under high pressure. Since the ionic radius of Fe^{2+} (~0.63 Å) is moderate, either K_2CuCl_3-typed or K_2AgI_3-typed structure of Ba_2FeS_3 can be stabilized depending on its synthesis method. As shown in Fig. 3, contrasted with the arrangement of paired BaS_7 polyhedrons in K_2CuCl_3-typed Ba_2FeS_3(AP), the chain-like configurations of BaS_7 polyhedrons in K_2AgI_3-typed Ba_2FeS_3(HP) form a tighter structure in the *ac*-plane; while it is stretched along the *b* axis, which causes the FeS_4 tetrahedron more distorted as seen in Table 2. Since high pressure tends to make the compounds condensed and allow higher tolerance factor, K_2AgI_3-typed Ba_2FeS_3(HP) can be stabilized via the synthesis of high-pressure method. Finally, we list the ratios of $r_{M^{2+}}/r_{Ba^{2+}}$ and the structure type for a series of Ba_2MS_3 (*M* = Mn, Fe, Co, Zn, Hg, Cd) compounds in Table 3.

3.2. Physical properties

To study the oxidation state of the Fe ions in Ba_2FeS_3(HP) and Ba_2FeS_3(AP), we have performed soft x-ray absorption spectroscopy (SXAS) experiments at the Fe-$L_{2,3}$ edges. It is well-known that the line shape of the atomic-like multiplet features in the 3*d* transition-metal $L_{2,3}$ spectra is very sensitive to the valence and spin state as well as the local environment of the 3*d* ion [27–31]. The comparison of the Fe-$L_{2,3}$ spectra of Ba_2FeS_3(HP) and Ba_2FeS_3(AP) is shown in Fig. 4, where $Mg_{1-x}Fe_xO$ taken from reference (28) and CaFeSeO taken from reference (31) are used as Fe^{2+} reference and Fe_2O_3 as Fe^{3+} reference. First, we can observe that the spectra of Ba_2FeS_3(HP) and Ba_2FeS_3(AP) are very similar to each other. Second, the spectra of these two compounds are shifted by more than 1 eV to lower

Table 3
The r_M/r_{Ba} ratios for a series of Ba_2MS_3 (*M* = Mn, Fe, Co, Zn, Hg, Cd) compounds.

Ba_2MS_3	Radius of *M* (Å)	r_M/r_{Ba}	Structure
Ba_2CoS_3	0.58	0.420	K_2CuCl_3-type
$Ba_2Co_{0.5}Zn_{0.5}S_3$	0.59	0.428	K_2CuCl_3-/K_2AgI_3-type
Ba_2ZnS_3	0.60	0.435	K_2CuCl_3-/K_2AgI_3-type
Ba_2FeS_3	0.63	0.456	K_2CuCl_3-/K_2AgI_3-type
Ba_2MnS_3	0.66	0.478	K_2AgI_3-type
Ba_2CdS_3	0.78	0.565	K_2AgI_3-type
Ba_2HgS_3	0.96	0.700	K_2AgI_3-type

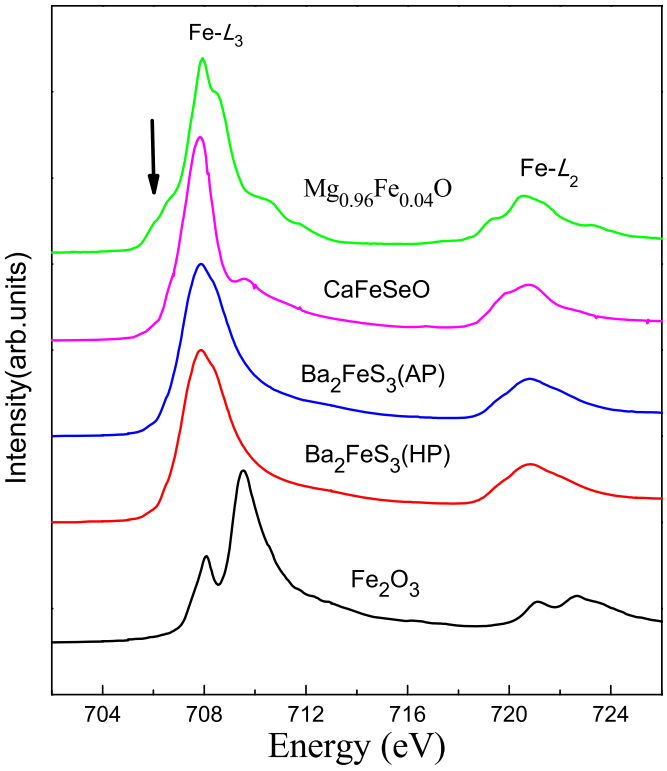

Fig. 4. Fe-$L_{2,3}$ XAS spectra of Ba_2FeS_3(HP) and Ba_2FeS_3(AP) together with those of Fe_2O_3 as a Fe^{3+} reference, $Mg_{0.96}Fe_{0.04}O$ [28] and CaFeSeO as the Fe^{2+} references [31].

energies with respect to the spectrum of Fe_2O_3 while they are at the same energy as that of $Mg_{1-x}Fe_xO$ and CaFeSeO, which indicates that the Fe ions are divalent (+2) in both Ba_2FeS_3(HP) and Ba_2FeS_3(AP). There is, however, a clear difference in comparison with $Mg_{1-x}Fe_xO$, especially the shoulder below the main peak of the Fe-L_3 edge of $Mg_{1-x}Fe_xO$, reflecting indeed the different local coordination, namely tetrahedral local symmetry in the Ba_2FeS_3(HP) and Ba_2FeS_3(AP) versus octahedral in $Mg_{1-x}Fe_xO$ [28]. In fact, the Ba_2FeS_3 spectra are more similar to the one of CaFeSeO since the Fe in the latter compound is also tetrahedrally coordinated by two oxygens and two selenium atoms [31]. Third, the spectra of Ba_2FeS_3(HP) and Ba_2FeS_3(AP) exhibit multiplet-like spectral features, especially at the Fe-L_2 edge, suggesting localization of their 3*d* electrons.

The temperature dependence of resistivity of both Ba_2FeS_3(HP) and Ba_2FeS_3(AP) is presented in Fig. 5. For both samples, the resistivity increases with decreasing temperature, thereby demonstrating a semiconducting behavior. The resistivity at 380 K is about 1.4×10^3 Ω-cm for Ba_2FeS_3(HP) and 0.7×10^3 Ω-cm for Ba_2FeS_3(AP). The inset shows the curves of ln(ρ) versus 1/*T*. The straight line in the whole experimental temperature range suggests that the semiconducting behavior can be described based on the Arrhenius law for thermally activated conduction. By using the formula, $\rho \propto exp\ (\triangle_g/2k_BT)$, where $\triangle_g$ is the semiconducting band gap and k_B is the Boltzmann's constant, the resistivity curves were well fitted and $\triangle_g$ were obtained to be 676 meV and 608 meV for Ba_2FeS_3(HP) and Ba_2FeS_3(AP), respectively. The value of $\triangle_g$ for Ba_2FeS_3(AP) obtained here agrees with the previous work reported by W. M. Reiff [32]. Ba_2FeS_3(HP) has a larger band gap, which suggests that intrachain distance d_{intra} plays a key role and determines the resistivity since Ba_2FeS_3(HP) has a larger value of d_{intra}.

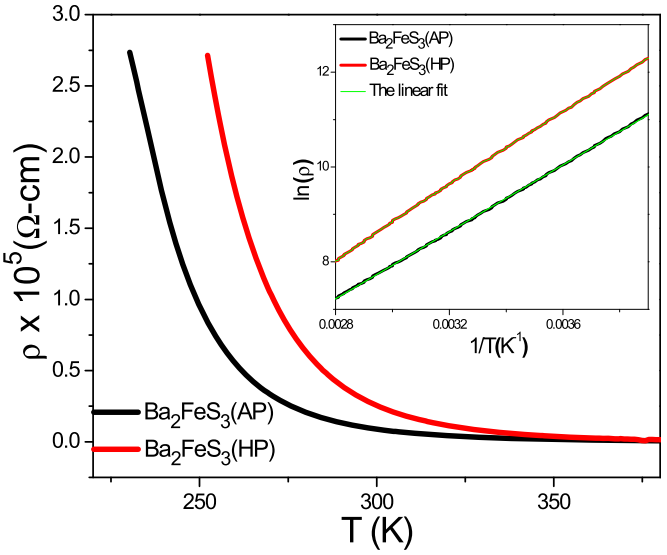

Fig. 5. Temperature dependence of resistivity for the sample of Ba_2FeS_3(HP) and Ba_2FeS_3(AP). The inset is the plot of ln(ρ) versus inverse temperature.

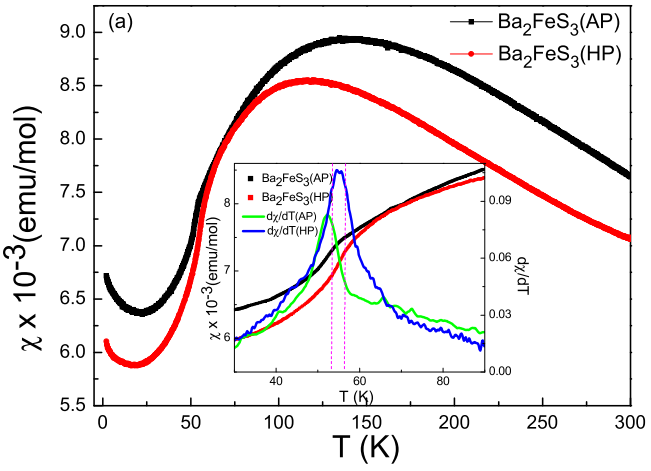

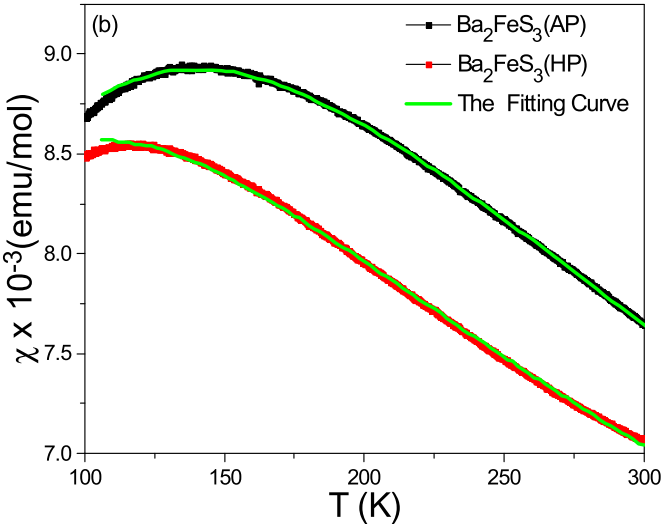

Fig. 6. (a) Temperature dependence of magnetic susceptibility for Ba_2FeS_3(HP) and Ba_2FeS_3(AP) measured under the magnetic field of 1000 Oe. The inset presents the enlarged view and the differential curves $d(\chi)/dT$ vs T to demonstrate the magnetic ordering transition. The green curve is $d(\chi)/dT$ vs T for Ba_2FeS_3(AP), and the blue is for Ba_2FeS_3(HP). (b) The enlarged view of susceptibility with the temperature range from 100 K to 300 K and the fitting curve using the Wagner-Friedberg model. (For interpretation of the references to colour in this figure legend, the reader is referred to the Web version of this article.)

In order to explore the magnetic properties, the *dc* magnetic susceptibility measurement was carried out with the applied field of 1000 Oe as shown in Fig. 6(a). For Ba_2FeS_3(HP), there is a round hump at 110 K, where the susceptibility reaches the maximum. The round hump characteristic should arise from the short-range antiferromagnetic spin coupling, which is a typical behavior expected for quasi 1D antiferromagnetic compounds. Below the maximum temperature (T_{max}), the susceptibility drops as temperature decreases, and a small kink can be observed at 56 K. To clearly display the anomaly, we plotted the temperature derivative of resistivity, as shown in the inset of Fig. 6(a). When temperature decreases further, the susceptibility goes up at ~20 K due to paramagnetic impurities. While for Ba_2FeS_3(AP), the susceptibility exhibits a similar shape with that of Ba_2FeS_3(HP) but with a higher T_{max} ~130 K and lower kink temperature of 54 K. The hump feature with T_{max} ~130 K in Ba_2FeS_3(AP) agrees with the previous work reported by N. Nakayama [33]. In their work, the antiferromagnetic ground state was confirmed by MÖssbauer Spectra experiments, however, the ordering temperature was not determined from the previous magnetic susceptibility measurement due to limited resolutions. Beside Ba_2FeS_3(AP), Ba_2CoS_3 and Ba_2MnS_3 with the similar chain structure also were reported to exhibit a broad round magnetic susceptibility associated with the short antiferromagnetic coupling at 125 K and 100 K, respectively [33]. What is more, Ba_2CoS_3 was found to form long-range antiferromagnetic ordering, which is signed by a small anomaly at 46 K in both the susceptibility and specific heat data [34]. Therefore, the kinks in the susceptibilities of both Ba_2FeS_3(HP) and Ba_2FeS_3(AP) are speculated to arise from the long-range antiferromagnetic order transitions, which will be confirmed by the specific heat measurements.

In addition, we find that the behavior of the magnetic susceptibilities in the high temperature regime cannot be described by Curie-Weiss law due to the intrachain antiferromagnetic fluctuation, which has been reported in Ba_2CoS_3 with the similar chain structure [34]. Here, we use the Wagner-Friedberg model to fit our magnetic susceptibility data, which was proved to work for different spin chains [35–39]. Wagner and Friedberg extended the Fisher's model to the case of spin values different from 1/2 with the following formula:

$$\chi = \frac{N\mu_B{}^2 g^2 S(S+1)}{3k_B T} \frac{1-U(T_0/T)}{1+U(T_0/T)}$$

where $T_0 = 2J_{intra}S(S+1)$, $U(x) = \coth(x) - 1/x$, g is Landé constant, N is the Avogadro number, S is the spin moment and J_{intra} is the intrachain interaction. Here, J_{intra} for antiferromagnetic coupling is defined as negative. It should be noted that the Wagner-Friedberg model cannot be used to fit the low temperature regime with $T < T_{max}$. After fitting to the high temperature susceptibility, as presented in Fig. 6(b), the obtained intrachain coupling J_{intra} is about −18 K and −24 K and g value 2.2 and 2.4 for Ba_2FeS_3(HP) and Ba_2FeS_3(AP), respectively. Also, we can estimate the J_{intra} values via the mean-field approximation with the equation of $k_B\theta = 2z(S(S+1))J/3$, where θ is the temperature associated with intrachain coupling strength and can be coarsely replaced with the maximum

temperature T_{max}, $z = 2$ is the coordinate number and $S = 2$ is the spin moment for Fe^{2+}. Thus, the value of J_{intra} for Ba_2FeS_3(HP) and Ba_2FeS_3(AP) can be calculated to be about −14 K and −16 K, respectively. Because of the strong magnetic fluctuation in quasi 1D spin chains, the value of Θ is underestimated if T_{max} is used here. Therefore, the intrachain interaction J_{intra} obtained from mean-field approximation is somehow lower than that from Wagner-Friedberg model.

Fig. 7(a) and (b) presents the temperature dependence of specific heat $C_p(T)$ for Ba_2FeS_3(HP) and Ba_2FeS_3(AP), respectively. In addition, we plotted the C_p/T vs T curves (shown in Fig.S1). No anomaly is observed near the maximum temperature T_{max}, where a round hump associated with the short-range antiferromagnetic coupling can be seen in the magnetic susceptibility. While there is a small kink at 56 K and 54 K for Ba_2FeS_3(HP) and Ba_2FeS_3(AP), respectively, which confirms that there happens a long-range magnetic ordering transition. Since the specific heat jump at the Néel temperature is very weak, the magnetic entropy around the ordering temperature should be very small. This weak anomaly in specific heat is generally observed in quasi 1D spin chain system

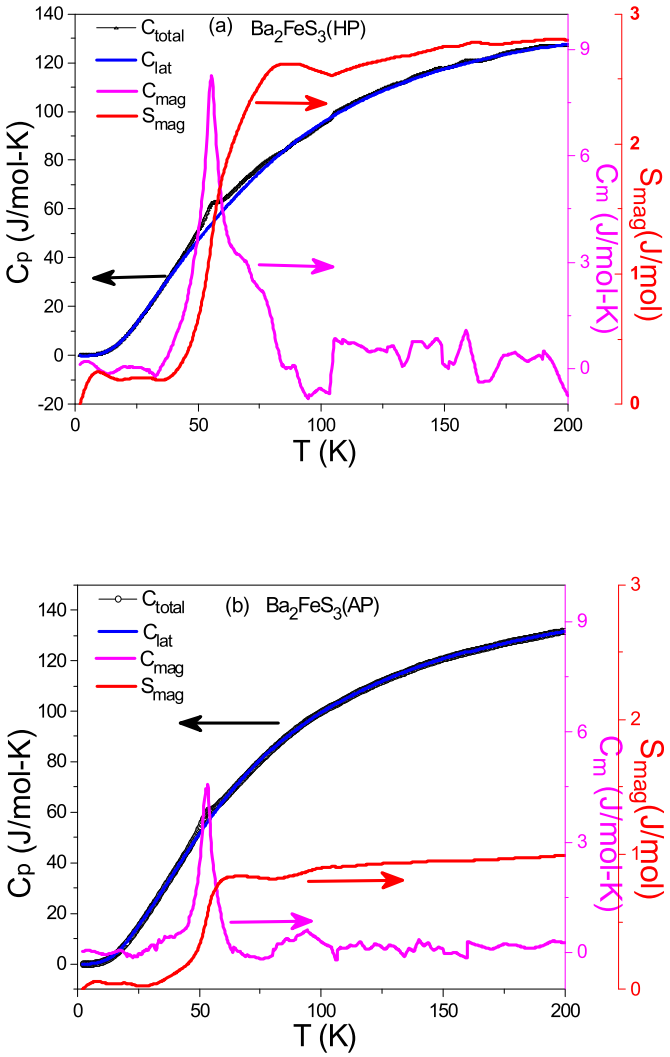

Fig. 7. Specific heat data for (a) Ba_2FeS_3(HP) and (b) Ba_2FeS_3(AP). The blue line is the fit using the combination of Debye model and Einstein model. The purple curve denotes the magnetic contribution to the specific heat and the red line is the magnetic entropy. (For interpretation of the references to colour in this figure legend, the reader is referred to the Web version of this article.)

because most of the magnetic entropy has been released via intrachain spin correlation above the long-range magnetic ordering transition. For example, in the compound of $Ba_9V_3Se_{15}$ with quasi 1D ferrimagnetic chain, the long-range ordering temperature is ~2.5 K, above which a large magnetic contribution to the specific heat has been observed due to the 1D spin wave excitation [40]. To extract the magnetic entropy, we first fit the specific heat data by combining the Debye model and Einstein model to give the lattice contribution $C_{lattice}$ as shown with the blue curve. After subtracting the contribution of lattice, the magnetic contribution C_{mag} can be obtained, as seen with the purple curve. The temperature dependence of C_{mag} exhibits a sharp peak at the Néel temperature. Finally, we can get the magnetic entropy through the integration of C_{mag}/T over the whole temperature range, which is shown with the red line. The total magnetic entropy change ΔS caused by the long-range ordering transition is ~2.8 J/mol-K and ~1.0 J/mol-K for Ba_2FeS_3(HP) and Ba_2FeS_3(AP), respectively, which is only 7−20 % of the expected value $R*\ln(2S+1) = 13.4$ J/mol-K for a $S = 2$ system. In addition, the C_p/T vs T^2 curves below 20 K were fitted by the formula $C_p(T)/T = \gamma + [\beta T^2 + \sigma T^4 + \theta T^6]$, where the first term respects the contributions of the electronic specific heat (SH) and the last three terms for phonon contribution (shown in Fig. S2 (a) and (b)). The Debye temperature Θ_D can be derived from the value of parameter β to be 301.1 K and 246.6 K for Ba_2FeS_3(HP) and Ba_2FeS_3(AP), respectively, according to the formula $\Theta_D = (12\pi^4 Rn/5\beta)^{1/3}$, where $n = 6$ is the number of atoms in the unit cell.

From above results we can see that both Ba_2FeS_3(HP) and Ba_2FeS_3(AP) exhibit strong 1D features. In their crystal structures, the intrachain distance of Fe ions d_{intra} is smaller than the interchain distance d_{inter}. In addition, the Fe ions in the chain are connected with S^{2-} anions and the super-exchange interaction between intrachain spins is mediated via S^{2-} anions; while the interchain Fe ions are separated by the polyhedral BaS_7. Thereby, it is suggested that the intrachain spin coupling J_{intra} should be much stronger than the interchain coupling J_{inter}. For a quasi 1D spin chain system, the long-range magnetic ordering is governed by J_{inter} although it generally is one or two orders of magnitude smaller than J_{intra}. Before the long-range ordering formation, the intrachain spins correlation has pre-developed. In both of the compounds, the antiferromagnetic intrachain spin correlation happens above the ordering temperature, which causes a round hump behavior seen in their magnetic susceptibility and leads to a small magnetic entropy change near the magnetic ordering temperature. Furthermore, due to the similar spin chain structure, we can compare the one dimensionality between Ba_2FeS_3(HP) and Ba_2FeS_3(AP). First, the distance of adjacent intrachain Fe^{2+} ions $d_{intra} = 4.2973\ (1)$ Å in Ba_2FeS_3(HP) is larger than Ba_2FeS_3(AP) ($d_{intra} = 4.2494\ (1)$ Å); while the interchain distance of the nearest neighbor Fe ions in Ba_2FeS_3(HP) $d_{inter} = 5.5199\ (0)$ Å is much smaller than that of 6.2123 (1) Å in Ba_2FeS_3(AP). Second, compared with Ba_2FeS_3(AP) ($T_N = 54\ K$ and $T_{max} \sim 130\ K$), the magnetic ordering temperature $T_N = 56$ K for Ba_2FeS_3(HP), related to the interchain coupling strength of J_{inter}, is higher; while the round hump temperature $T_{max} \sim 110$ K seen in the magnetic susceptibility, coarsely responding to the value of J_{intra}, is lower. Third, the magnetic entropy loses due to the intrachain spin correlation pre-development in Ba_2FeS_3(HP) is smaller than that of Ba_2FeS_3(AP). All the above results indicate that both of the compounds are featured with 1D structure, while Ba_2FeS_3(HP) has a slightly weaker one-dimensionality than Ba_2FeS_3(AP).

4. Conclusions

We successfully synthesized a new phase of Ba_2FeS_3(HP) under high-pressure conditions, which crystallizes in a K_2AgI_3-typed orthorhombic structure with the space group of *Pnma* (62). The

crystal structure consists of chains of corner-sharing FeS_4 tetrahedra along the *b* axis, which are separated by Ba^{2+} ions. It is a semiconductor with the band gap about 676 meV and undergoes a long-range antiferromagnetic ordering transition at T_N ~56 K. Above T_N, the short-range antiferromagnetic intrachain spin correlation has pre-developed, which is featured by a round hump at T_{max} ~110 K seen in the magnetic susceptibility and a small magnetic contribution to the specific heat at T_N. Ba_2FeS_3(AP) also displays an antiferromagnetic ground state with T_N ~54 K. Our results indicate that both the compounds are featured with spin chains, contain FeS_4 tetrahedron complex and exhibit AFM ground state, which make them to be candidates to explore new superconductor with low dimensionality.

CRediT authorship contribution statement

Lei Duan: Formal analysis, Investigation, Data curation, Writing - original draft, Writing - review & editing, Visualization. **Jun Zhang:** Formal analysis, Data curation, Writing - original draft, Visualization. **Xiancheng Wang:** Conceptualization, Formal analysis, Writing - original draft, Writing - review & editing. **Zhiwei Zhao:** Formal analysis, Data curation. **Changjiang Xiao:** Formal analysis, Data curation. **Xiang Li:** Formal analysis, Writing - original draft. **Zhiwei Hu:** Formal analysis, Writing - original draft, Writing - review & editing. **Jianfa Zhao:** Data curation, Visualization. **Wenmin Li:** Data curation, Visualization. **Lipeng Cao:** Data curation, Visualization. **Guangyang Dai:** Investigation, Validation. **Chongwen Ren:** Investigation, Visualization. **Xin He:** Investigation, Validation. **Runze Yu:** Formal analysis, Supervision. **QingQing Liu:** Resources, Visualization. **Liu Hao Tjeng:** Investigation, Writing - review & editing. **Hong-Ji Lin:** Resources, Investigation. **Chien-Te Chen:** Resources, Investigation. **Changqing Jin:** Conceptualization, Project administration, Formal analysis, Writing - original draft, Resources.

Declaration of competing interest

The authors declare that they have no known competing financial interests or personal relationships that could have appeared to influence the work reported in this paper.

Acknowledgments

The present work was supported by the National Key R&D Program of China and the National Natural Science Foundation of China under grant no. 2018YFA0305700, 11974410, 11921004, 11820101003 and 2017YFA0302900, and the Doctoral Fund of Henan University of Technology under Grant No. 2020BS029. We acknowledge the support from the Max Planck-POSTECH-Hsinchu Center for Complex Phase Materials.

Appendix A. Supplementary data

Supplementary data to this article can be found online at https://doi.org/10.1016/j.jallcom.2020.157839.

References

[1] Y. Kamihara, T. Watanabe, M. Hirano, H. Hosono, Iron-based layered superconductor La[$O_{1-x}F_x$]FeAs (x=0.05-0.12) with *Tc* = 26 K, J. Am. Chem. Soc. 130 (2008) 3296.
[2] M. Rotter, M. Tegel, D. Johrendt, Superconductivity at 38 K in the iron arsenide ($Ba_{1-x}K_x$)Fe_2As_2, Phys. Rev. Lett. 101 (2008) 107006.
[3] X.C. Wang, Q.Q. Liu, Y.X. Lv, W.B. Gao, L.X. Yang, R.C. Yu, F.Y. Li, C.Q. Jin, The superconductivity at 18 K in LiFeAs system, Solid State Commun. 148 (2008) 538–540.
[4] F.C. Hsu, J.Y. Luo, K.W. Yeh, T.K. Chen, T.W. Huang, P.M. Wu, Y.C. Lee, Y.L. Huang, Y.Y. Chu, D.C. Yan, M.K. Wu, Superconductivity in the PbO-type structure alpha-FeSe, Proc Natl Acad Sci U S A/PNAS 105 (2008) 14262–14264.
[5] K. Ishida, Y. Nakai, H. Hosono, To what extent iron-pnictide new superconductors have been clarified: a progress report, J. Phys. Soc. Jpn. 78 (2009), 062001.
[6] Q.S. Wang, Y. Shen, B.Y. Pan, Y.Q. Hao, M.W. Ma, F. Zhou, P. Steffens, K. Schmalzl, T.R. Forrest, M. Abdel-Hafiez, X.J. Chen, D.A. Chareev, A.N. Vasiliev, P. Bourges, Y. Sidis, H.B. Cao, J. Zhao, Strong interplay between stripe spin fluctuations, nematicity and superconductivity in FeSe, Nat. Mater. 15 (2016) 159.
[7] J. Guo, S. Jin, G. Wang, S. Wang, K. Zhu, T. Zhou, M. He, X. Chen, Superconductivity in the iron selenide $K_xFe_2Se_2$($0 \le x \le 1.0$), Phys. Rev. B 82 (2010) 180520.
[8] C.-H. Li, B. Shen, F. Han, X. Zhu, H.-H. Wen, Transport properties and anisotropy of $Rb_{1-x}Fe_{2-y}Se_2$ single crystals, Phys. Rev. B 83 (2011) 184521.
[9] X. Dong, H. Zhou, H. Yang, J. Yuan, K. Jin, F. Zhou, D. Yuan, L. Wei, J. Li, X. Wang, G. Zhang, Z. Zhao, Phase diagram of (Li(1-x)Fe(x))OHFeSe: a bridge between iron selenide and arsenide superconductors, J. Am. Chem. Soc. 137 (2015) 66–69.
[10] H. Takahashi, Pressure-induced superconductivity in the iron based ladder material $BaFe_2S_3$, Nat. Mater. 14 (2015) 1008.
[11] T. Yamauchi, Y. Hirata, Y. Ueda, K. Ohgushi, Pressure-Induced mott transition followed by a 24-K superconducting phase in $BaFe_2S_3$, Phys. Rev. Lett. 115 (2015) 246402.
[12] J. Ying, H. Lei, C. Petrovic, Y. Xiao, V.V. Struzhkin, Interplay of magnetism and superconductivity in the compressed Fe-ladder compound $BaFe_2Se_3$, Phys. Rev. B 95 (2017) 241109.
[13] Y. Zhang, L. Lin, J.-J. Zhang, E. Dagotto, S. Dong, Pressure-driven phase transition from antiferromagnetic semiconductor to nonmagnetic metal in the two-leg ladders AFe_2X_3 (A=Ba, K; X=S, Se), Phys. Rev. B 95 (2017) 115154.
[14] K. Takubo, Y. Yokoyama, H. Wadati, S. Iwasaki, T. Mizokawa, T. Boyko, R. Sutarto, F.Z. He, K. Hashizume, S. Imaizumi, T. Aoyama, Y. Imai, K. Ohgushi, Orbital order and fluctuations in the two-leg ladder materials $BaFe_2X_3$ (X = S and Se) and $CsFe_2Se_3$, Phys. Rev. B 96 (2017) 115157.
[15] J.P. Hu, Identifying the genes of unconventional high temperature superconductors, Sci. Bull. 61 (2016) 561–569.
[16] C.Q. Jin, Using pressure effects to create new emergent materials by design, MRS Advances 2 (2017) 2587–2596.
[17] W. Li, L. Cao, J. Zhao, X. Wang, R. Yu, Y. Long, Q. Liu, C. Jin, Superconductivity of a cuprate with compressed local octahedron, Sci. China Phys. Mech. Astron. 62 (2019), 037421.
[18] L. Duan, J. Zhang, X. Wang, J. Zhao, L. Cao, W. Li, Z. Deng, R. Yu, Z. Li, C. Jin, High-pressure synthesis, structure and properties of new ternary pnictides La_3TiX_5 (X = P, As), J. Alloys Compd. 831 (2020) 154697.
[19] W.M. Li, J.F. Zhao, L.P. Cao, Z. Hu, Q.Z. Huang, X.C. Wang, Y. Liu, G.Q. Zhao, J. Zhang, R.Z. Yu, Q.Q. Liu, Y.W. Long, H. Wu, H.J. Lin, C.T. Chen, Z. Li, Z.Z. Gong, Z. Guguchia, J.S. Kim, G.R. Stewart, Y.J. Uemura, S. Uchida, C.Q. Jin, Superconductivity in a unique type of copper oxide, Proc Natl Acad Sci U S A/PNAS 116 (2019) 12156–12160.
[20] J. Zhang, Y. Jia, X. Wang, Z. Li, L. Duan, W. Li, J. Zhao, L. Cao, G. Dai, Z. Deng, S. Zhang, S. Feng, R. Yu, Q. Liu, J. Hu, J. Zhu, C. Jin, A new quasi-one-dimensional compound Ba_3TiTe_5 and superconductivity induced by pressure, NPG Asia Mater. 11 (11) (2019) 60.
[21] H.Y. Hong, H. Steinfink, The crystal chemistry of phase in the Ba-Fe-S and Se systems, J. Solid State Chem. 5 (1972) 93–104.
[22] C.Q. Jin, S. Adachi, X.J. Wu, H. Yamauchi, S. Tanaka, 117-K superconductivity in the Ba-Ca-Cu-O system, Physica C 223 (1994) 238–242.
[23] C.Q. Jin, X.J. Wu, P. Laffez, T. Tatsuki, T. Tamura, S. Adachi, H. Yamauchi, N. Koshizuka, S. Tanaka, Superconductivity at 80 K in $(Sr,Ca)_3Cu_2O_{4+\delta}Cl_{2-y}$ induced by apical oxygen doping, Nature 375 (1995) 301–303.
[24] M.A. Greaney, K.V. Ramanujachary, Z. Teweldemedhin, M. Greenblatt, Studies on the linear-chain antiferromagnets - Ba_2MnX_3 (X=S, Se, Te) and their solid-solutions, J. Solid State Chem. 107 (1993) 554–562.
[25] S. Hull, P. Berastegui, Crystal structures and ionic conductivities of ternary derivatives of the silver and copper monohalides—II: ordered phases within the $(AgX)_x$–$(MX)_{1-x}$ and $(CuX)_x$–$(MX)_{1-x}$ (*M* = K, Rb and Cs; *X* =Cl, Br and I) systems, J. Solid State Chem. 177 (2004) 3156–3173.
[26] F. Mezzadri, E. Gilioli, G. Calestani, A. Migliori, M.R. Harrison, D.A. Headspith, M.G. Francesconi, Using high pressure to prepare polymorphs of the $Ba_2Co_{1-x}Zn_xS_3$ ($0 \le x \le 1.0$) compounds, Inorg. Chem. 51 (2012) 397–404.
[27] T. Burnus, Z. Hu, H. Wu, J.C. Cezar, S. Niitaka, H. Takagi, C.F. Chang, N.B. Brookes, H.J. Lin, L.Y. Jang, A. Tanaka, K.S. Liang, C.T. Chen, L.H. Tjeng, X-ray absorption and x-ray magnetic dichroism study on Ca_3CoRhO_6 and Ca_3FeRhO_6, Phys. Rev. B 77 (2008) 205111.
[28] T. Haupricht, R. Sutarto, M.W. Haverkort, H. Ott, A. Tanaka, H.H. Hsieh, H.J. Lin, C.T. Chen, Z. Hu, L.H. Tjeng, Local electronic structure of Fe^{2+} impurities in MgO thin films: temperature-dependent soft x-ray absorption spectroscopy study, Phys. Rev. B 82 (2010), 035120.
[29] N. Hollmann, Z. Hu, M. Valldor, A. Maignan, A. Tanaka, H.H. Hsieh, H.J. Lin, C.T. Chen, L.H. Tjeng, Electronic and magnetic properties of the kagome systems $YBaCo_4O_7$ and $YBaCo_3MO_7$ (M=Al, Fe), Phys. Rev. B 80 (2009), 085111.
[30] N. Hollmann, M. Valldor, H. Wu, Z. Hu, N. Qureshi, T. Willers, Y.Y. Chin, J.C. Cezar, A. Tanaka, N.B. Brookes, L.H. Tjeng, Orbital occupation and magnetism of tetrahedrally coordinated iron in $CaBaFe_4O_7$, Phys. Rev. B 83 (2011), 180405(R).

[31] K.T. Lai, A.C. Komarek, M.T. Fernandez-Diaz, P.S. Chang, S. Huh, H. Rosner, C.Y. Kuo, Z. Hu, T.W. Pi, P. Adler, V. Ksenofontov, L.H. Tjeng, M. Valldor, Canted antiferromagnetism on rectangular layers of Fe(2+) in polymorphic CaFeSeO, Inorg. Chem. 56 (2017) 4271–4279.

[32] W.M. Reiff, I.E. Grey, A. Fan, Z. Eliezer, H. Steinfink, Oxidation-state of iron in some Ba-Fe-S phases - mossbauer and electrical-resistivity investigation of Ba_2FeS_3, $Ba_7Fe_6S_{14}$, $Ba_6Fe_8S_{15}$, $BaFe_2S_3$, and $Ba_9Fe_{16}S_{32}$, J. Solid State Chem. 13 (1975) 32–40.

[33] N. Nakayama, K. Kosuge, S. Kachi, T. Shinjo, T. Takada, Studies on the compounds in the Ba-Fe-S system .1. Linear-chain antiferromagnetism of Ba_2FeS_3 and related-compounds Ba_2CoS_3 and Ba_2MnS_3, J. Solid State Chem. 33 (1980) 351–356.

[34] A.D.J. Barnes, T. Baikie, V. Hardy, M.B. Lepetit, A. Maignan, N.A. Young, M.G. Francesconi, Magnetic coupling and long-range order in the spin-chain sulfide Ba_2CoS_3, J. Mater. Chem. 16 (2006) 3489–3502.

[35] A.C. Gandhi, R. Das, F.C. Chou, J.G. Lin, Magnetocrystalline two-fold symmetry in $CaFe_2O_4$ single crystal, J. Phys. Condens. Matter : an Institute of Phys. Journal 29 (2017) 175802.

[36] J. Zhang, L. Duan, Z. Wang, X.C. Wang, J.F. Zhao, M.L. Jin, W.M. Li, C.L. Zhang, L.P. Cao, Z. Deng, Z.W. Hu, S. Agrestini, M. Valvidares, H.-J. Lin, C.-T. Chen, J.L. Zhu, C.Q. Jin, The synthesis of a quasi-one-dimensional iron-based telluride with antiferromagnetic chains and a spin glass state, Inorg. Chem. 59 (2020) 5377–5385.

[37] E.A. Popova, A.N. Vasiliev, V.L. Temerov, L.N. Bezmaternykh, N. Tristan, R. Klingeler, B. Buchner, Magnetic and specific heat properties of $YFe_3(BO_3)_4$ and $ErFe_3(BO_3)_4$, J. Phys. Condens. Matter : an Institute of Physics journal 22 (2010) 116006.

[38] L.D. Sanjeewa, V.O. Garlea, M.A. McGuire, C.D. McMillen, H. Cao, J.W. Kolis, Structural and magnetic characterization of the one-dimensional S=5/2 antiferromagnetic chain system $SrMn(VO_4)(OH)$, Phys. Rev. B 93 (2016) 224407.

[39] Y. Zhang, X.T. Wang, X.M. Zhang, T.F. Liu, W.G. Xu, S. Gao, Synthesis, structures, and magnetism of three 1D Mn(III) chains with oxazoline-based ligands, Inorg. Chem. 49 (2010) 5868–5875.

[40] J. Zhang, M. Liu, X.C. Wang, K. Zhao, L. Duan, W.M. Li, J.F. Zhao, L.P. Cao, G.Y. Dai, Z. Deng, S.M. Feng, S.J. Zhang, Q.Q. Liu, Y.F. Yang, C.Q. Jin, $Ba_9V_3Se_{15}$: a novel compound with spin chains, J. Phys. Condens. Matter 30 (2018) 214001.